Exact Feedback Linearization of a Multi-Variable Controller for a Bi-Directional DC-DC Converter as Interface of an Energy Storage System

Gabriel R Broday, Luiz a C Lopes, Gilney Damm

energies

MDPI

Article

Exact Feedback Linearization of a Multi-Variable Controller for a Bi-Directional DC-DC Converter as Interface of an Energy Storage System

Gabriel R. Broday [1], Luiz A. C. Lopes [1,*] and Gilney Damm [2]

[1] Department of Electrical and Computer Engineering, Concordia University, Montreal, QC H3G 1M8, Canada
[2] Department of Components and Systems (COSYS), University Gustave Eiffel, 93162 Paris, France
* Correspondence: lalopes@encs.concordia.ca

Abstract: DC microgrids have shown to be a good approach for better accommodating stochastic renewable energy sources (RES) and for the charging of electric vehicles (EVs) at the distribution level. For this, fast-acting energy storage units (ESSs) are essential. This requires that both the bi-directional power converter topology and the control scheme present the right set of features. The ESS discussed in this paper consists of a new DC-DC converter based on a tapped inductor (TI) for a higher voltage gain at moderate duty cycles. The direction of the current in its intermediate inductor does not need to be reversed for power flow reversal, leading to a faster action. Moreover, it can employ a multi-state and multi-variable modulation scheme that eliminates the right half-plane (RHP) zero, common in boost-type converters. In order to achieve good dynamic performance across a wide range of operating points, a control scheme based on feedback linearization is developed. This paper presents the modeling of the five-switch DC-DC converter operating in the tri-state buck–boost mode. A systematic approach for deriving control laws for the TI current and output voltage based on exact state feedback linearization is discussed. The performance of the proposed control scheme is verified by simulation for a supercapacitor (SC)-based ESS. It is compared to that of a conventional control scheme for a dual-state buck–boost mode with cascaded PI controllers designed based on small-signal models. The results show that both control schemes work similarly well at the operating point that the conventional control scheme was designed for. However, only the proposed scheme allows the SC-based ESS to control the current injected into the DC microgrid with the voltage of the SC varying between the expected range of rated to half-rated.

Keywords: exact feedback linearization; multi-variable controller; bi-directional DC-DC converter; energy storage systems

Citation: Broday, G.R.; Lopes, L.A.C.; Damm, G. Exact Feedback Linearization of a Multi-Variable Controller for a Bi-Directional DC-DC Converter as Interface of an Energy Storage System. *Energies* **2022**, *15*, 7923. https://doi.org/10.3390/en15217923

Academic Editor: Alon Kuperman

Received: 19 September 2022
Accepted: 20 October 2022
Published: 25 October 2022

1. Introduction

The decentralization of power generation has become a topic of high interest for industry and academia. The integration of stochastic renewable energy sources (RESs) at the distribution level is facilitated by incorporating them into a microgrid [1]. DC microgrids are a good option since many RESs (photovoltaic and fuel cells) and energy storage units present DC output characteristics [2]. The efficiency of the DC-DC interfaces tends to be higher than in DC-AC, and issues such as frequency regulation, reactive power control and synchronization are avoided [3,4]. The control of segments of the distribution system as a microgrid also helps with the deployment of new large loads, such as electric vehicles (EVs). However, fast-acting energy storage systems (ESSs) are essential for balancing supply and demand, thus regulating the DC bus voltage [5–7].

The power converters of the ESSs must be bi-directional and can be either isolated or non-isolated. The dual-active bridge (DAB) is an example of the former, allowing higher voltage gains than the latter at the expense of a higher switch count. Among the non-isolated bi-directional DC-DC converters, there are the Class C and the four-switch

converter, with two half-bridges and an intermediate inductor. The relatively low voltage gains of these topologies can be increased with topologies that employ tapped inductors (TIs) [8]. In [9], a three-switch converter with a TI is discussed. By employing a tri-state modulation scheme, the right half-plane (RHP) zero that appears in the control-to-output transfer function of the converters can be eliminated, thus increasing the speed of response of the converter [9,10]. It should be noted that for the three topologies mentioned above, the current in the intermediate inductor must be reversed for power flow reversal, which slows down the operation. In [11], a five-switch bi-directional DC-DC converter that does not present this constraint was presented. Moreover, it can also operate with tri-state modulation for an improved dynamic response [12].

Power converters frequently employ linear PI-type controllers [13,14]. They are designed based on converter models linearized around a specific operating point. The performance of PI controllers tends to degrade if the operating point of the converter changes. This might be a significant issue for ESSs that are prone to wide variations in the output current, as well as for the input voltage, when supercapacitors (SCs) are used as storage units. Recall that SCs typically operate with voltages in the range of rated to half-rated. For cases such as this, state feedback linearization techniques are a good and effective alternative. State feedback linearization has been applied to unidirectional buck, boost and buck–boost converters in [15–17], respectively. It was also applied to a bi-directional Class C converter in [18,19], and to a four-switch converter in [20]. One potential issue in these cases is when the inductor current is used as a feedback term in the denominator of the control law. Note that this quantity crosses zero during power flow reversal, leading to a potential singularity. The above converters are all single-input single-output (SISO) systems, but the technique has also been applied to multi-input multi-output (MIMO) systems. In [21], exact feedback linearization was used in a three-port boost converter for interfacing a PV panel to a battery and load. In [22], it was applied to a four-level buck converter with two flying capacitors and an LC output filter. Suitable control laws were developed to generate the duty cycles of the three switches so as to regulate three of the four state variables.

In this paper, state feedback linearization is applied to a new bi-directional DC-DC converter with a TI for an increased voltage gain at moderate duty cycles. A multi-state modulation scheme with multiple modulation signals is used to eliminate the RHP zero typically found in converters with intermediate inductors. Unlike previously reported DC-DC converters, this one allows reversal of the power flow without reversing the intermediate inductor current. This is beneficial since the inductor current, which is often used in the denominator of the control laws, will always be positive, eliminating potential singularities. It is a dual-input dual-output (DIDO) system, which is the simplest form of a MIMO system, where the magnitude of the inductor current presents a certain degree of independence with regard to the output voltage. In principle, it can be adjusted as a trade-off between converter losses and the speed of response of the output voltage.

This paper is organized as follows. In Section 2, the five-switch bi-directional DC-DC converter is introduced. Section 3 presents the modeling of the system for both power flow directions, and how they are combined into a single model. Section 4 presents the derivation of the control law of the converter based on state feedback linearization, while Section 5 presents the system parameters, with considerations for controller design. The performance of the five-switch converter operating in the tri-state buck–boost mode with state feedback by means of simulation is verified in Section 6. It also presents a comparison with the conventional dual-state buck–boost with cascaded inner current outer voltage loops with linear PI controllers. Finally, Section 7 provides the final conclusion of this research work.

2. The Five-Switch Bi-Directional DC-DC Converter

The bi-directional DC-DC converter considered in this paper is shown in Figure 1. It consists of five switches interfacing two DC buses, Bus 1 and Bus 2, through a TI. This

is modeled as an ideal transformer with two windings (L_{T1} and L_{T2}) and a magnetizing inductance (L_M) in parallel with the primary winding. The turns ratio of the windings, L_{T1}/L_{T2}, is $n/1$. The converter can present a high voltage gain (V_2/V_1) in the conventional dual-state scheme without an overly high duty cycle, by properly selecting the turns ratio n [23]. Capacitors C_1 and C_2 are low-pass input and output filters. The energy storage unit, in Bus 1, and cabling to the converter, as well as the DC microgrid, are modeled by a voltage source in series with a resistor (V_1–R_1 and V_2–R_2).

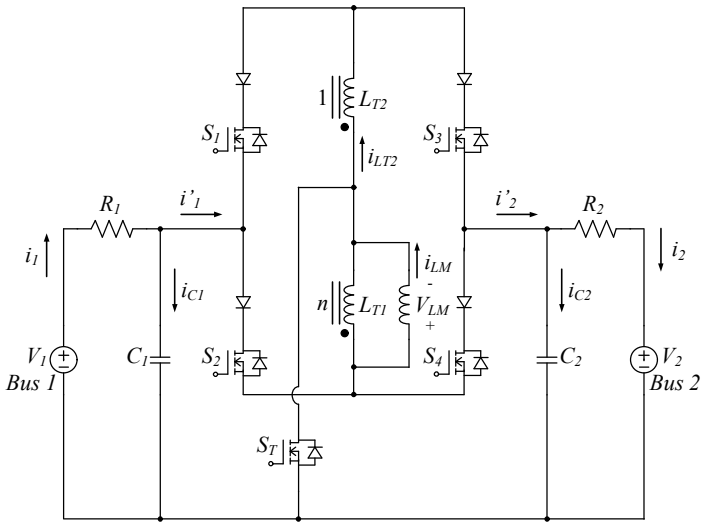

Figure 1. The 5-switch bi-directional DC-DC converter.

For the proper operation of the power converter, switches S_1 to S_4 should be unidirectional in terms of current, such as those used in PWM current source inverters (CSIs): IGBTs with reverse blocking capability or IGBTs/MOSFETs in series with a diode. Conversely, S_T (the switch that taps the inductor to the common node of the DC buses) is a standard MOSFET with an anti-parallel body diode for bi-directional current flow. The converter allows a number of paths for the inductor current, or states of operation, as shown in Table 1. State S_{XY} concerns a moment when switches S_X and S_Y are on/activated together. They can be used in a switching cycle with two or three states [12,23]. Circuit current and voltage waveforms are also presented in [12,23]. Power flow reversal occurs without changing the direction of the current in the magnetizing inductance (i_{LM}), favoring a fast dynamic response.

Table 1. Possible states of operation.

State	Current Path	i'_1	i'_2	v_{LM}	Power Flow
S_{2T}	S_2 and S_T	i_{LM}	0	$v_{C1} > 0$	Bus 1 to inductor
S_{4T}	S_4 and S_T	0	$-\,i_{LM}$	$v_{C2} > 0$	Bus 2 to inductor
S_{3T}	S_3 and $D(S_T)$ *	0	$n\,i_{LM}$	$-n\,v_{C2}$	Inductor to Bus 2
S_{1T}	S_1 and $D(S_T)$ *	$-n\,i_{LM}$	0	$-n\,v_{C1}$	Inductor to Bus 1
S_{23}	S_2 and S_3	$(n\,i_{LM})/(n+1)$	$(n\,i_{LM})/(n+1)$	$(n\,v_{C1} - n\,v_{C2})/(n+1)$	Bus 1 to Bus 2
S_{14}	S_1 and S_4	$(-n\,i_{LM})/(n+1)$	$(-n\,i_{LM})/(n+1)$	$(n\,v_{C2} - n\,v_{C1})/(n+1)$	Bus 2 to Bus 1
S_{34}	S_3 and S_4	0	0	0	Free-wheeling (fw)
S_{12}	S_1 and S_2	0	0	0	Free-wheeling (fw)

* $D(S_T)$ refers to the anti-parallel body diode of S_T.

Based on the operating states and current paths presented in Table 1, Figures 2 and 3 present the current paths, highlighted in red, for all possible operating states for each power flow direction.

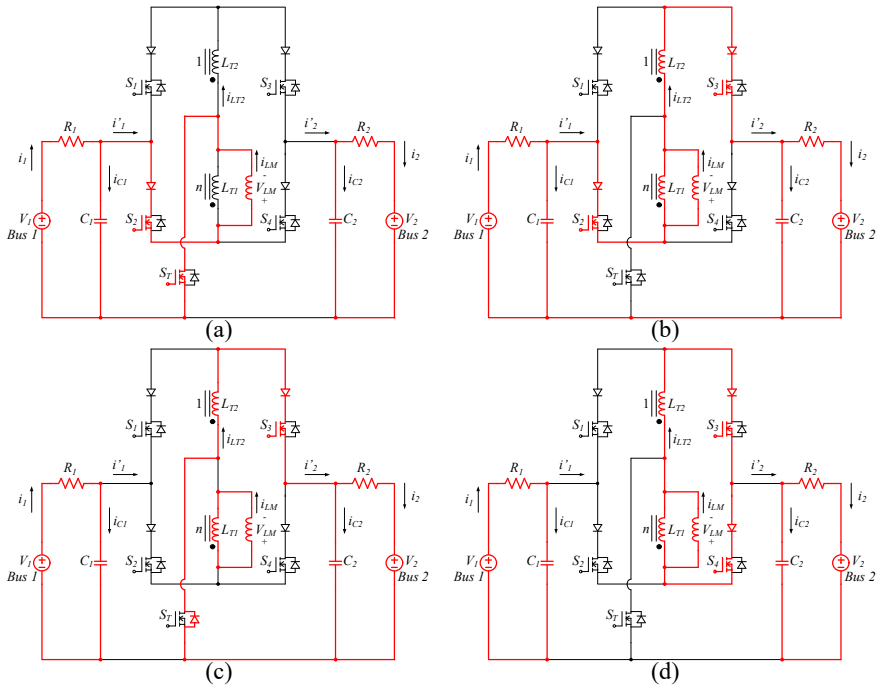

Figure 2. Current paths (in red) for the operating states of the forward mode. (**a**) State S_{2T}; (**b**) State S_{23}; (**c**) State S_{3T}; (**d**) State S_{34}.

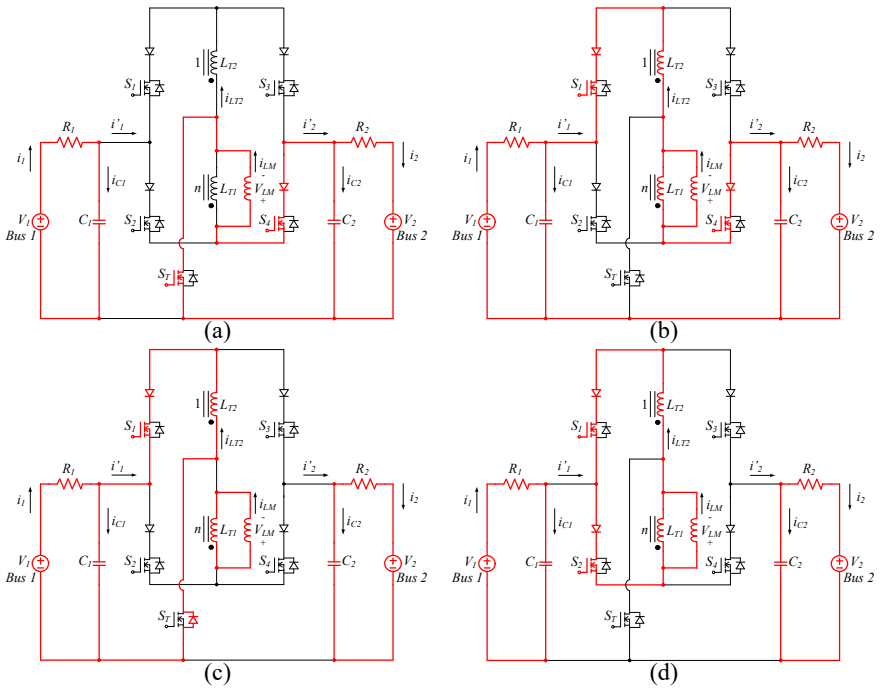

Figure 3. Current paths (in red) for the operating states of the reverse mode. (**a**) State S_{4T}; (**b**) State S_{14}; (**c**) State S_{1T}; (**d**) State S_{12}.

The converter can operate in the dual-state modes [10] and in the tri-state modes [11]. The tri-state buck–boost mode is selected for this paper. In the forward mode, with power flowing from Bus 1 to Bus 2, states S_{2T}, S_{3T} and S_{34} are used. Conversely, in the reverse mode, states S_{4T}, S_{1T} and S_{12} are used. The PWM modulator for this type of operation is shown in Figure 4. It employs two modulation signals, m_1 and m_2, where the magnitude of m_2 is larger than of m_1 and an auxiliary signal (q) that determines the direction of the power

flow: $q = 1$ in the forward direction and $q = 0$ in the reverse direction. This modulator is used for obtaining the gating signals for the switches in both forward and reverse modes, shown in Figures 5 and 6.

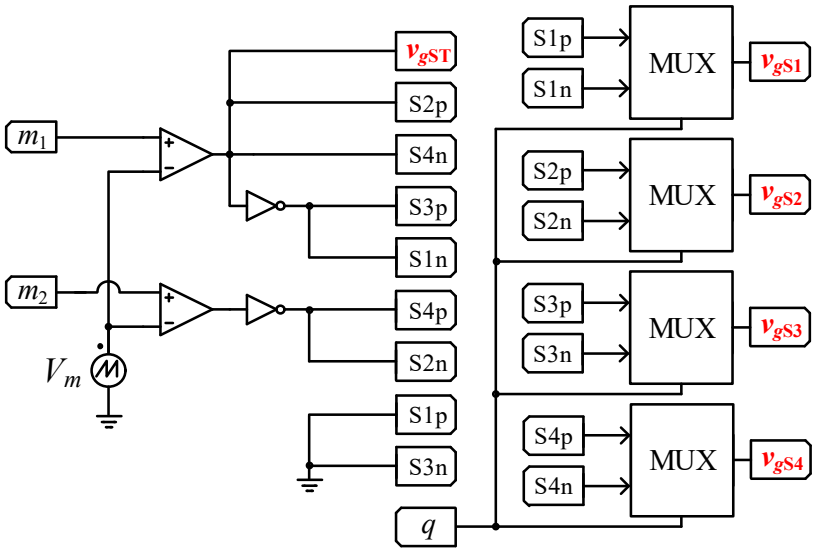

Figure 4. PWM modulator for the tri-state buck–boost mode of operation.

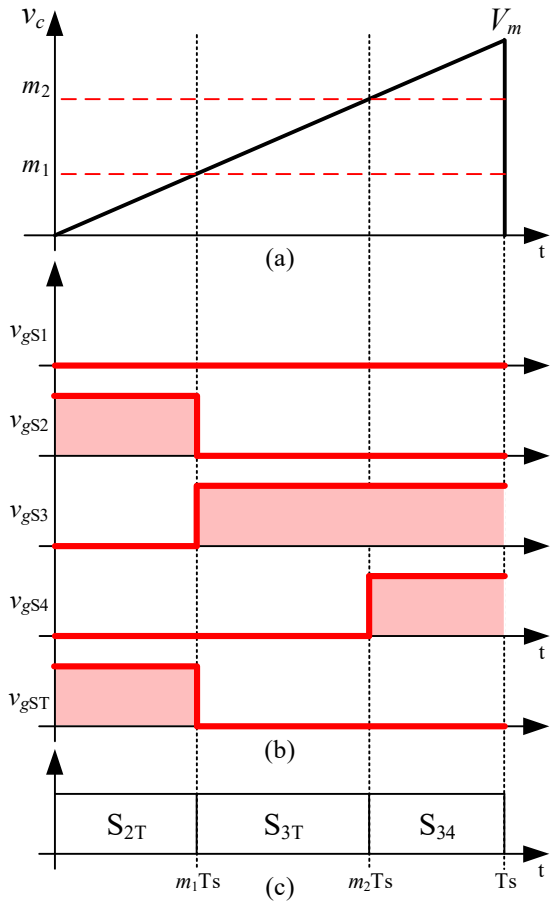

Figure 5. Forward mode: the carrier-based modulation scheme. (**a**) Carrier and modulating signals; (**b**) gating signals of the switches; (**c**) states of operation.

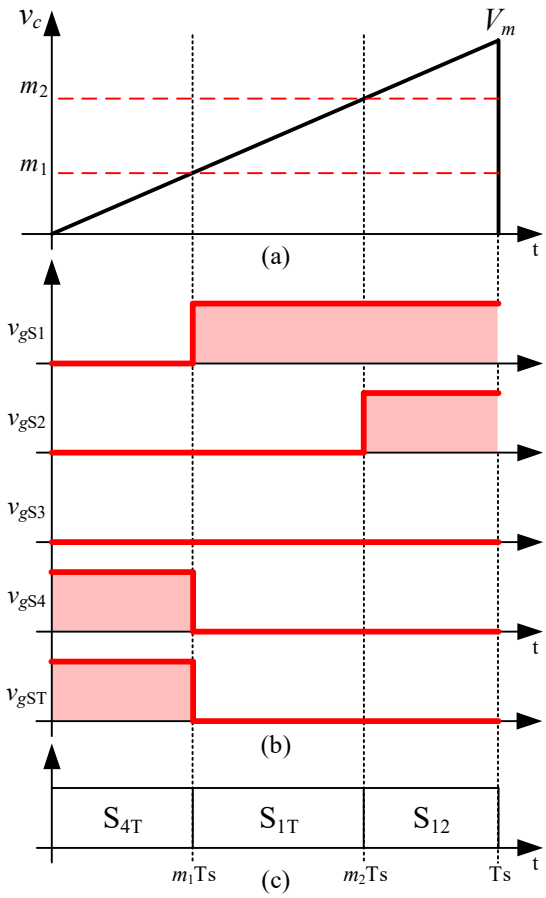

Figure 6. Reverse mode: the carrier-based modulation scheme. (**a**) Carrier and modulating signals; (**b**) gating signals of the switches; (**c**) states of operation.

The impact of the modulation signals (m_1 and m_2) on the gating signals of the switches (v_{gS1}–v_{gST}) and the duration of the states for tri-state buck–boost operation is illustrated in Figures 5 and 6, respectively, for the forward and reverse modes. There, one can see that a switching period consists of three states among those shown in Table 1. Assuming that the peak value of the sawtooth carrier (V_m) is 1 V, and that $m_1 < m_2 \leq 1$, the duty cycle of state $S_{2T} = D_{2T} = m_1$. Likewise, $D_{3T} = (m_2 - m_1)$ and $D_{34} = (1 - m_2)$. In the second segment, m_1T_s to m_2T_s, when only S_3 is on, the inductor current flows through S_3 and the body diode of S_T, sending energy from the inductor to Bus 2. For the reverse mode, $D_{4T} = m_1$, $D_{1T} = (m_2 - m_1)$ and $D_{12} = (1 - m_2)$. According to Table 1, these are equivalent states to those in the forward mode. For instance, in the second segment, m_1T_s to m_2T_s, when only S_1 is on, the inductor current flows through S_1 and the body diode of S_T, sending energy from the inductor to Bus 1.

3. Modeling of the Five-Switch Converter

In this section, the modeling of the converter is performed based on the analysis of the operating states that are generated by the PWM modulator for both the forward and reverse modes. The objective is to find a model that describes the system behavior as a function of the control variables m_1, m_2 and q. It is based on the differential equations of the three state variables of the bidirectional power converter: current in the magnetizing inductance (i_{LM}) and voltages across the filter capacitors (v_{C1} and v_{C2}).

By applying KVL and KCL for the three states of operation and averaging them for the forward mode, one obtains

$$\frac{di_{LM}}{dt} = \frac{v_{C1}}{L_M}(m_1) - \frac{n\,v_{C2}}{L_M}(m_2 - m_1) \tag{1}$$

$$\frac{dv_{C1}}{dt} = \frac{V_1}{R_1C_1} - \frac{v_{C1}}{R_1C_1} - \frac{i_{LM}}{C_1}(m_1) \tag{2}$$

$$\frac{dv_{C2}}{dt} = \frac{V_2}{R_2C_2} - \frac{v_{C2}}{R_2C_2} + \frac{n\,i_{LM}}{C_2}(m_2 - m_1) \tag{3}$$

Repeating the process for the reverse mode, one obtains

$$\frac{di_{LM}}{dt} = -\frac{n\,v_{C1}}{L_M}(m_2 - m_1) + \frac{v_{C2}}{L_M}(m_1) \tag{4}$$

$$\frac{dv_{C1}}{dt} = \frac{V_1}{R_1C_1} - \frac{v_{C1}}{R_1C_1} + \frac{n\,i_{LM}}{C_1}(m_2 - m_1) \tag{5}$$

$$\frac{dv_{C2}}{dt} = \frac{V_2}{R_2C_2} - \frac{v_{C2}}{R_2C_2} - \frac{i_{LM}}{C_2}(m_1) \tag{6}$$

By multiplying (1)–(3) by q and (4)–(6) by $\overline{q}$ and adding them, one obtains a final averaged model, valid for both forward and reverse modes:

$$\frac{di_{LM}}{dt} = \dot{i_{LM}} = \frac{v_{C1}}{L_M}(u_2) - \frac{v_{C2}}{L_M}(u_1) \tag{7}$$

$$\frac{dv_{C1}}{dt} = \dot{v_{C1}} = \frac{V_1}{R_1C_1} - \frac{v_{C1}}{R_1C_1} - \frac{i_{LM}}{C_1}(u_2) \tag{8}$$

$$\frac{dv_{C2}}{dt} = \dot{v_{C2}} = \frac{V_2}{R_2C_2} - \frac{v_{C2}}{R_2C_2} + \frac{i_{LM}}{C_2}(u_1) \tag{9}$$

where the new control variables, u_1 and u_2, are defined as

$$u_1 = (m_2 - m_1)nq - m_1\overline{q} \tag{10}$$

$$u_2 = m_1q - (m_2 - m_1)n\overline{q} \tag{11}$$

4. Exact State Feedback Linearization

The non-linear characteristics of this system can be observed in the model developed in the previous section. It includes cross-products between the state variables and the new control variables u_1 and u_2. Using the conventional linearization approach based on small signal variations around an operating point to design conventional PI controllers, information would be lost and the system would not be fully described by the resulting model.

The main goal of an ESS is usually to control the output current, i_2, which can be achieved indirectly through the output voltage, v_{C2}. Frequently, this is achieved by employing a cascaded inner inductor current and outer output voltage control loop. However, since the developed model presents two control variables, u_1 and u_2, and in order to give more flexibility to the considered non-linear controller, this paper implements a parallel control structure. In this case, the inductor current reference can be chosen according to the system needs, with high values favoring a faster dynamic response and lower ones for improved efficiency.

The first step of the controller design is to rewrite the DIDO system, presented in Figure 7, in an affine linear form to apply the theory of exact state feedback linearization. This is achieved by means of (12) and (13).

$$\dot{x} = f(x) + g(x)u \tag{12}$$

$$y = h(x) \tag{13}$$

where $x \in \mathbb{R}^n$ is the state vector; $u \in \mathbb{R}^m$. relates to the control inputs; $y \in \mathbb{R}^i y$ defines the controlled outputs; f, g and h are differentiable vector fields. Considering the model developed in the last section,

$$x = [i_{LM}, v_{C1}, v_{C2}]^t = [x_1, x_2, x_3]^t \tag{14}$$

$$u = [u_1, u_2]^t \tag{15}$$

$$f(x) = \left[0, \frac{V_1}{R_1 C_1} - \frac{x_2}{R_1 C_1}, \frac{V_2}{R_2 C_2} - \frac{x_3}{R_2 C_2}\right]^t \tag{16}$$

$$g(x) = \begin{bmatrix} -\frac{x_3}{L_M} & \frac{x_2}{L_M} \\ 0 & -\frac{x_1}{C_1} \\ \frac{x_1}{C_2} & 0 \end{bmatrix}, g_1(x) = \left[-\frac{x_3}{L_M}, 0, \frac{x_1}{C_2}\right]^t, g_2(x) = \left[\frac{x_2}{L_M}, -\frac{x_1}{C_1}, 0\right]^t \tag{17}$$

$$h_1(x) = x_1 = [1,0,0];\ h_2(x) = x_3 = [0,0,1] \tag{18}$$

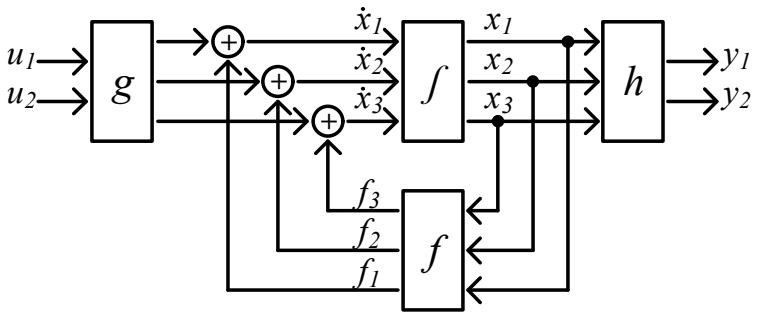

Figure 7. Block diagram representation of the DIDO system.

There are several methods for obtaining the feedback linearization of the DIDO system [24–27]. First, the model is rewritten in a different set of coordinates, using the output y and its successive derivatives. This procedure is performed based on Equation (13), obtaining

$$\dot{y}_i = L_f h_i + \sum_{j=1}^{m} (L_{gj} h_i) u_j \tag{19}$$

where $L_f h$ and $L_g h$ are, respectively, *Lie derivatives* of the smooth scalar vector $h(x)$ as a function of $f(x)$ and $g(x)$. If $L_{gj} h_i(x) = 0$ for all j, then the inputs do not appear, and, as highlighted by [22,24], one needs to differentiate repetitively as

$$y_i^{r_i} = L_f{}^{(r_i)} h_i + \sum_{j=1}^{m} \left(L_{gj} L_f^{r_i - 1} h_i\right) u_j \tag{20}$$

until $L_{gj} L_f^{r_i - 1} h_i \neq 0$ for at least one j. The values of r_i are the sub-relative degrees of the DIDO system, and $L_{gj} L_f^{r_i - 1} h_i$ is the *Lie derivative* of the i-th output as a function of $f(x)$ and $g(x)$ [22,24]. In such a case, (20) can be rewritten as

$$\begin{bmatrix} y_1^{r_1} \\ \cdots \\ y_i^{r_i} \end{bmatrix} = A(x) + E(x) \begin{bmatrix} u_1 \\ \cdots \\ u_2 \end{bmatrix} \tag{21}$$

where

$$A(x) = \begin{bmatrix} L_f^{r_1} h_1 \\ \cdots \\ L_f^{r_i} h_i \end{bmatrix} \tag{22}$$

and

$$E(x) = \begin{bmatrix} L_{g1} L_f^{r_1-1} h_1 & \cdots & L_{gm} L_f^{r_1-1} h_1 \\ \cdots & \cdots & \cdots \\ L_{g1} L_f^{r_i-1} h_i & \ldots & L_{gm} L_f^{r_i-1} h_i \end{bmatrix} \tag{23}$$

Matrix $E(x)$ is called the decoupling matrix of the DIDO system. If it is nonsingular, the following input transformation can be defined:

$$u = -E^{-1} A(x) + E^{-1}(x) z \tag{24}$$

where z concerns new input variables.

Substituting (24) into (21) results in a linear and decoupled differential relation between the output y and the new input z [19].

$$\begin{bmatrix} y_1^{r_1} \\ \cdots \\ y_i^{i} \end{bmatrix} = \begin{bmatrix} z_1 \\ \cdots \\ z_i \end{bmatrix} \tag{25}$$

It is important to remark that (21), or its closed loop (25), creates a new model for the converter. If this new state vector, represented by the original outputs and their derivatives, does not match the same number of states (n_s) of the original system, it means that this new mathematical model is not describing the dynamics of all states in the converter. As a consequence, any analysis based on this new model would disregard the remaining states. These are called the zero dynamics of this new representation. For a complete analysis of the converter, one must consider these new variables as well as these zero-dynamics.

Taking into account the 5-switch converter operating with the tri-state buck–boost mode with two control variables (u_1 and u_2) and two state variables to be controlled (i_{Lm} and v_{C2}), one can find the sub-relative degrees by considering $m = 2$ (two inputs) and $i = 1$ and 2 (two outputs).

By solving the Lie derivatives, one can find the sub-relative degrees of the system as follows.

For $y_1 = h_1 = x_1 = i_{Lm} = [1, 0, 0]$, then

$$\begin{cases} L_{g1} h_1 = [1\ 0\ 0] \left[-\frac{x_3}{L_M}, 0, \frac{x_1}{C_2} \right]^t = -\frac{x_3}{L_M} \\ L_{g2} h_1 = [1\ 0\ 0] \left[\frac{x_2}{L_M}, -\frac{x_1}{C_1}, 0 \right]^t = \frac{x_2}{L_M} \end{cases} \tag{26}$$

For $y_2 = h_2 = x_3 = v_{C2} = [0, 0, 1]$, then

$$\begin{cases} L_{g1} h_2 = [0\ 0\ 1] \left[-\frac{x_3}{L_M}, 0, \frac{x_1}{C_2} \right]^t = \frac{x_1}{C_2} \\ L_{g2} h_2 = [0\ 0\ 1] \left[\frac{x_2}{L_M}, -\frac{x_1}{C_1}, 0 \right]^t = 0 \end{cases} \tag{27}$$

Thus, the sub-relative degrees of the system are $r_1 = 1$ and $r_2 = 1$. Knowing these two values, it is possible now to fully define matrix $E(x)$ as

$$E(x) = \begin{bmatrix} L_{g1} L_f^{r_1-1} h_1 & L_{g2} L_f^{r_1-1} h_1 \\ L_{g1} L_f^{r_2-1} h_2 & L_{g2} L_f^{r_2-1} h_2 \end{bmatrix} = \begin{bmatrix} L_{g1} L_f^{0} h_1 & L_{g2} L_f^{0} h_1 \\ L_{g1} L_f^{0} h_2 & L_{g2} L_f^{0} h_2 \end{bmatrix} \tag{28}$$

Therefore, by replacing (26) and (27) with (28), matrix $E(x)$ is finally given by

$$E(x) = \begin{bmatrix} -\frac{x_3}{L_M} & \frac{x_2}{L_M} \\ \frac{x_1}{C_2} & 0 \end{bmatrix} \tag{29}$$

Next, one computes vector $A(x)$ as

$$A(x) = \begin{bmatrix} L_f^{r_1} h_1 \\ L_f^{r_2} h_2 \end{bmatrix} = \begin{bmatrix} L_f h_1 \\ L_f h_2 \end{bmatrix} \tag{30}$$

where

$$\begin{cases} L_f h_1 = \begin{bmatrix} 1 & 0 & 0 \end{bmatrix} \left[0, \frac{V_1}{R_1 C_1} - \frac{x_2}{R_1 C_1}, \frac{V_2}{R_2 C_2} - \frac{x_3}{R_2 C_2} \right]^t = 0 \\ L_f h_2 = \begin{bmatrix} 0 & 0 & 1 \end{bmatrix} \left[0, \frac{V_1}{R_1 C_1} - \frac{x_2}{R_1 C_1}, \frac{V_2}{R_2 C_2} - \frac{x_3}{R_2 C_2} \right]^t = \frac{V_2}{R_2 C_2} - \frac{x_3}{R_2 C_2} \end{cases} \tag{31}$$

Thus,

$$A(x) = \left[0, \frac{V_2}{R_2 C_2} - \frac{x_3}{R_2 C_2} \right]^t \tag{32}$$

With matrices $E(x)$ and $A(x)$ defined, one obtains the control law of the converter from (24) as

$$u = \begin{bmatrix} \frac{x_3 - V_2}{R_2 x_1} \\ \frac{x_3 (x_3 - V_2)}{R_2 x_1 x_2} \end{bmatrix} + \begin{bmatrix} 0 & \frac{C_2}{x_1} \\ \frac{L_M}{x_2} & \frac{x_3 C_2}{x_1 x_2} \end{bmatrix} z \tag{33}$$

It should be noted that, since, for this particular converter, $i_{LM} = x_1$ does not need to be reversed for power flow reversal and $v_{C1} = x_2 \approx V_1 > 0$ and $v_{C2} = x_3 \approx V_2 > 0$, there are no singularities in the linearized system. Particularizing (25) for this converter, one observes that the equivalent system is linear and decoupled, as shown in (34). It can be represented by a block diagram, as shown in Figure 8.

$$\begin{bmatrix} y_1^1 \\ y_2^1 \end{bmatrix} = \begin{bmatrix} \dot{i}_{Lm} \\ \dot{v}_{C2} \end{bmatrix} = \begin{bmatrix} z_1 \\ z_2 \end{bmatrix} \tag{34}$$

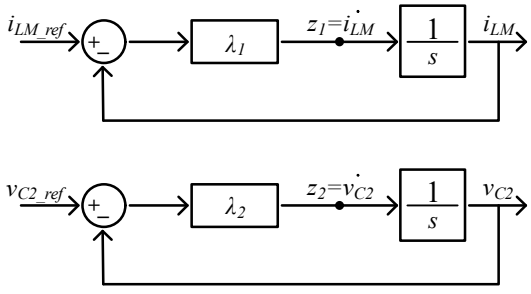

Figure 8. Linear decoupled model of the 5-switch converter.

For tracking reference values for i_{LM} and v_{C2}, given by i_{LM_ref} and v_{C2_ref}, respectively, one can use simple proportional controllers to obtain inputs z_1 and z_2 required in (34). This implies taking

$$\begin{aligned} z_1 &= -\lambda_1 \left(i_{LM} - i_{LM\_ref} \right) \\ z_2 &= -\lambda_2 \left(v_{C2} - v_{C2\_ref} \right) \end{aligned} \tag{35}$$

The overall system, with the original system, state feedback linearization network and simple proportional controllers, is shown in Figure 9. In general, the objective of the "control system" is to provide the modulation signals that will result in the tracking of some reference quantities. In this case, the modulation signals are m_1 and m_2 and the quantities to be tracked are $i_{LM} = x_1$ and $v_{C2} = x_3$. The modulation signals can be obtained from (10)

and (11), provided that u_1 and u_2, signals in the input of block "*system*" in Figure 9, are known. According to (33) and as depicted in Figure 9, u_1 and u_2 are functions of the state variables $i_{LM} = x_1$, $v_{C1} = x_2$ and $v_{C2} = x_3$, as well as z_1 and z_2. The latter are the outputs of the proportional controllers of the inductor current and output voltage loops, shown in Figure 8 and (35).

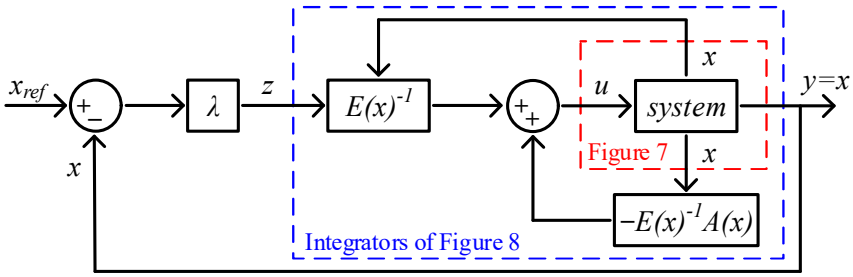

Figure 9. Model of the DIDO system with the state feedback linearization network and simple P-type controllers.

4.1. Remark: Tuning Guidelines

One interesting feature for the proposed control scheme is the fact that it relies on only two parameters, λ_1 and λ_2. These are indeed the desired closed-loop poles imposed by the control algorithm. They impose new dynamics to the closed-loop states represented by i_{LM} and v_{C2}, respectively. Their choice is completely straightforward; they directly impose the new time response of these variables. One can either choose them following practical considerations (desired time constant for these variables) or by a standard pole-placement procedure [28].

4.2. Zero Dynamics Analysis

Now, it is necessary to study the remaining dynamics of the system, the so-called zero dynamics. In the present case, they are trivial and are represented by the remaining state v_{C1}. For this analysis, one considers the dynamics when the controlled ones reach their equilibrium point. Then, the control amounts to (remark that $z = 0$ for this analysis)

$$\overline{u} = \begin{bmatrix} \frac{\overline{v_{C2}} - V_2}{R_2 \overline{i_{LM}}} \\ \frac{\overline{v_{C2}}(\overline{v_{C2}} - V_2)}{R_2 \overline{i_{LM}} x_2} \end{bmatrix} \tag{36}$$

and the zero-dynamics become

$$\dot{v_{C1}} = -\frac{v_{C1}}{R_1 C_1} - \frac{\overline{v_{C2}}(\overline{v_{C2}} - V_2)}{C_1 R_2 v_{C1}} + \frac{V_1}{R_1 C_1} \tag{37}$$

This system has two equilibrium points given by

$$v_{C1} = \frac{V_1}{2} \pm \sqrt{\frac{{V_1}^2}{4} - \overline{v_{C2}}(\overline{v_{C2}} - V_2)} \tag{38}$$

Only the larger solution is feasible. This one has as a Jacobian

$$-\frac{1}{R_1 C_1} + \frac{\overline{v_{C2}}(\overline{v_{C2}} - V_2)}{C_1 R_2} \left(\frac{V_1}{2} + \sqrt{\frac{{V_1}^2}{4} - \overline{v_{C2}}(\overline{v_{C2}} - V_2)} \right)^{-2} \tag{39}$$

This is negative inside a large operation region. Hence, the zero dynamics are asymptotically stable in this region, and, consequently, the full system is asymptotically stable.

5. System Parameters

The application scenario for the performance verification of the five-switch converter with the proposed control scheme is as an interface between two DC buses/elements, as depicted in Figure 1. It is assumed that the values of V_2 and R_2 are known. The rated voltages were taken as V_1 = 96 V and V_2 = 380 V and the rated power 1.9 kW. Other converter parameters are as follows: turns ratio n = 2, L_M = 38.8 µH, C_1 = 76.8 µF, C_2 = 76.8 µF, and f_{sw} = 250 kHz. The feeder resistances are R_1 = 0.0625 Ω and R_2 = 0.0625 Ω. These parameters are similar to those used in [12,23], which discuss the power electronic aspects of the five-switch DC-DC converter. The gains (λ_1 and λ_2) of the non-linear controller with state feedback linearization for the converter operating in tri-state buck–boost mode were computed, based on pole placement from linear control theory, as 250 k and 350 k, respectively. These gains are computed taking into account the behavior of a first-order system, where they relate to the time constant (T_s) of such systems. In this case, $T_{s\_\lambda 1}$ = 16 µs and $T_{s\_\lambda 2}$ = 11.4 µs.

In order to demonstrate the feasibility and benefits of the proposed mode of operation, tri-state buck–boost, and state feedback linearization, its performance is compared in the next section with a conventional technique. Usually, a converter such as this operates in dual-state buck–boost mode with a cascaded inner current (i_{LM}) and outer voltage (v_{C2}) control loop, as presented in Figure 10.

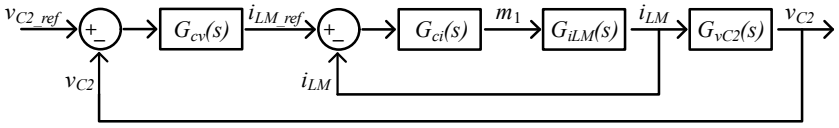

Figure 10. Block diagram of the cascaded control.

The small-signal model is obtained by means of the standard linearization of (7)–(9). For operation in dual-state buck–boost mode, considering the modulation schemes discussed in Section 2, one has to set m_2 to 1 V, to eliminate the free-wheeling states (S_{34} for the forward mode and S_{12} for the reverse mode), and then control the converter with a single input, m_1. The value of q is set at 1, since the forward power flow, boost mode, is the worst case concerning the design of the PI controller. With m_1 as the control variable, m_2 = 1 and q = 1, one substitutes (10)–(11) into (7)–(9) to obtain new state equations as a function of a single control variable: m_1. Then, one employs the conventional linearization technique, based on small-signal variations around a base operating point, to obtain transfer functions ($i_{LM}(s)/m_1(s)$ and $v_{C2}(s)/i_{LM}(s)$). The first can be found to be

$$G_{iLM}(s) = \frac{i_{LM}(s)}{m_1(s)} = \frac{[R_2C_2(V_{C1} + nV_{C2})]s + [n^2R_2(1-m_1)I_{LM} + V_{C1} + nV_{C2}]}{(R_2C_2L_M)s^2 + (L_M)s + n^2R_2(1-m_1)^2} \quad (40)$$

It is used for designing the PI-type controller of the inner current loop for zero error in steady state to step changes. For the design of the outer voltage control loop, considering that its bandwidth is 10–20% of the one for the inner current loop, the latter can be assumed to be a unity gain. Next, one can derive an expression for $v_{C2}(s)/i_{LM}(s)$), applying the current division principle that relates the current in the output capacitor ($i_{C2}(s)$) to $i_{LM}(s)$. This results in

$$i_{C2}(s) = ni_{LM}(s)(1-m_1) - i_2(s) = ni_{LM}(s)(1-m_1) - \frac{v_{C2}(s) - V_2}{R_2} \quad (41)$$

Finally, by assuming that V_2 remains constant, one can compute the transfer function of the output capacitor voltage over the inductor current as

$$G_{vC2}(s) = \frac{v_{C2}(s)}{i_{LM}(s)} = \frac{nR_2(1-m_1)}{(R_2C_2)s + 1} \quad (42)$$

In this particular case, standard type-2 PI controllers can be designed to provide the chosen bandwidths and phase margins for the inner and outer control loops. The parameters of the linear PI controllers were computed as follows. For the inner current loop, the bandwidth is selected as 50 kHz with a phase margin of 60°, resulting in K_{pi} = 0.0427, τ_i = 11.88 µs and f_{pi} = 186.7 kHz. For the outer voltage loop, the bandwidth is chosen as 10 kHz with a phase margin of 60°, leading to K_{pv} = 75.43, τ_v = 12.62 µs and fp_v = 7.93 kHz.

In Figure 11, the Bode diagrams of the linear cascaded control presented in Figure 10 are shown. From this figure, one can see that the compensated systems (orange plots) present the desired bandwidths and phase margin characteristics, validating the design of the type-2 PI controllers employed in the control law.

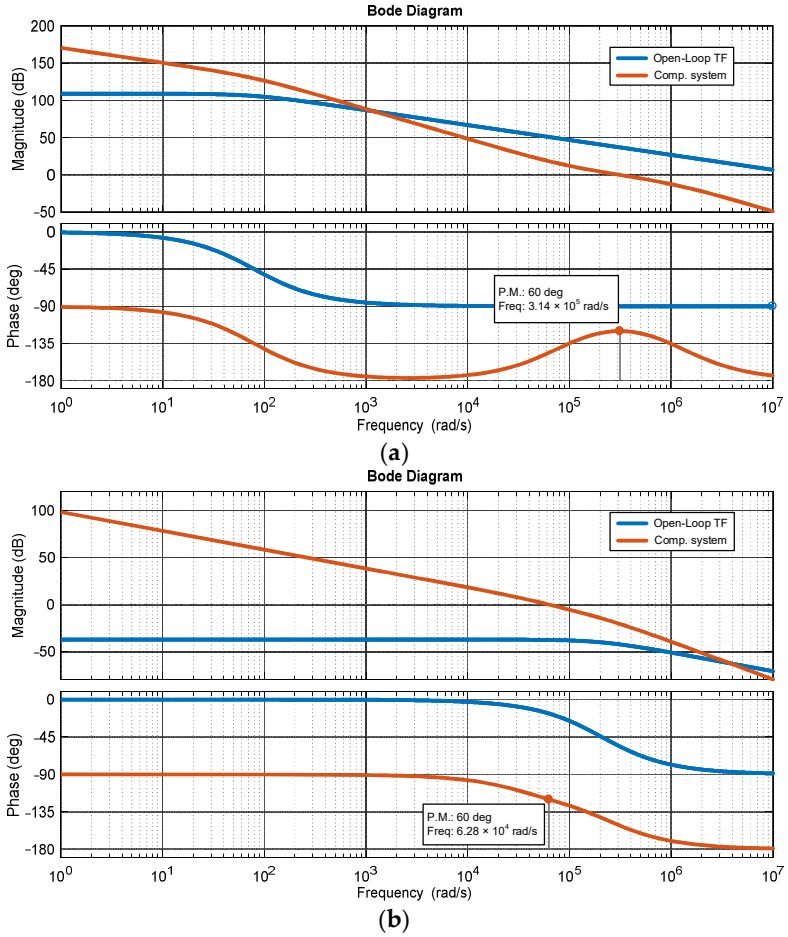

Figure 11. Bode plots of the linear controllers. (**a**) Current control loop, (**b**) voltage control loop.

6. Performance Verification

Two types of tests were conducted, by means of simulations with PSIM, to demonstrate the feasibility and the advantages of the proposed five-switch converter operating in tri-state buck–boost, with a non-linear control scheme based on state feedback linearization. First, it is assumed that the input (V_1) and output (V_2) voltages are kept constant at 96 V and 380 V, respectively. The output current reference signal (i_{2_ref}) is a square waveform of ±5 A and 5 Hz. This can be seen as the case where the five-switch converter (and control law) acts as an interlink converter between two strongly regulated DC buses, meaning that their voltages remain constant regardless of the power injected into, or withdrawn from, the DC buses. This can be considered as the base case. Here, the main goal is to verify whether one can control the output current (i_2) that is injected from one bus to another.

Next, an SC is used in Bus 1 (V_1) to work as a storage unit for a controlled DC microgrid, which is defined in Bus 2 (V_2) for this case study. SCs are devices with high power density and high charge/discharge rates that can be used to provide sudden bursts of power by managing currents with high gradients. Typically, the voltage on an SC is allowed to vary between half-rated and rated values. For the DC microgrid side, to emulate the power variations inherent to a DC microgrid, a sinusoidal ripple of 20 V (peak-to-peak) with a frequency of 120 Hz is added to the voltage source V_2, meaning that instead of staying constant at 380V, this voltage source will vary from 370 V to 390 V. This is a typical condition and concerns the connection of a DC bus to an AC bus (grid or load) through a single-phase DC-AC interface, where such an interface creates DC-side current and voltage harmonics at two times (120 Hz) the grid frequency (60Hz). This case might present a challenge for the performance of the conventional PI controllers, designed for a fixed operating point. Conversely, the non-linear control scheme with state feedback linearization should be able to compensate for these conditions, presenting similar behavior in a wide range of operating points. For this test, the same output current profile from the previous case is used.

Finally, the efficiency of the five-switch DC-DC converter operating in the tri-state buck–boost mode at rated conditions, V_1 = 96 V and V_2 = 380 V, with the output current varying from −5 A (reverse mode) to 5 A (forward mode), is investigated.

6.1. Tests with Fixed Values of V_1 and V_2

Figure 12 shows some key waveforms concerning the operation of the proposed non-linear controller with a fixed voltage at Bus 1 (Figure 12a) and Bus 2 (Figure 12b). In Figure 12c, one sees that the output current (i_2) follows the reference signal (i_{2_ref}). This is achieved indirectly by controlling the output voltage of the converter (v_{C2}), as shown in Figure 12d. The reference (i_{LM_ref}) and inductor current (i_{LM}) are shown in Figure 12e. There, one sees that i_{LM} tracks i_{LM_ref} very well and that power flow reversal, with i_2 changing from −5 A to 5 A, can be obtained without reversing i_{LM}. Moreover, the control of the two state variables, v_{C2} and i_{LM}, is achieved in a decoupled way, as discussed in Section 4. It is worth pointing out that the i_{LM_ref} is kept at 30 A until t = 0.25 s, when it is changed to 40 A, and then changed back to 30 A at t = 0.35 s. This action has two goals. The first is to show the good tracking capability of the inductor current control loop to step changes. A change in i_{2_ref} has a minor effect on i_{LM}. The second is to show the impact of the magnitude of i_{LM} on the values of the modulation signals, as discussed below. The waveforms of control variables (u_1 and u_2), which include the flag "q" with the direction of the power flow, are shown in Figure 12f. Those concerning the modulation signals (m_1 and m_2) used in the PWM modulator can be seen in Figure 12g. They remain within the range of the sawtooth carrier, 0 to 1 V, as expected. There, one can see that as i_{LM_ref} increases, the magnitude of the modulation signals (m_1 and m_2) decreases.

In general, no major difference can be seen between the two control schemes regarding the control of the output current (i_2) in Figures 12c and 13c. Both control schemes present fast and accurate tracking of the output current reference (i_{2_ref}). However, this is achieved with different values for the i_{LM}; see Figures 12e and 13e. For the conventional cascaded control scheme, the inductor current reference i_{LM_ref} varies with the output voltage reference (v_{C2_ref}). When the power flow is reversed, at t = 0.3 s and t = 0.4 s, i_{LM} also changes, but it remains always positive. This is a feature of the five-switch bi-directional DC-DC converter. Thus, i_{LM} and v_{C2} are coupled variables for the cascaded linear controller. Finally, Figure 13f shows that only one modulation signal, m_1, is used for both power flow directions for the converter operating in dual state with the conventional cascaded controller, while the other one, m_2, is kept at 1 V.

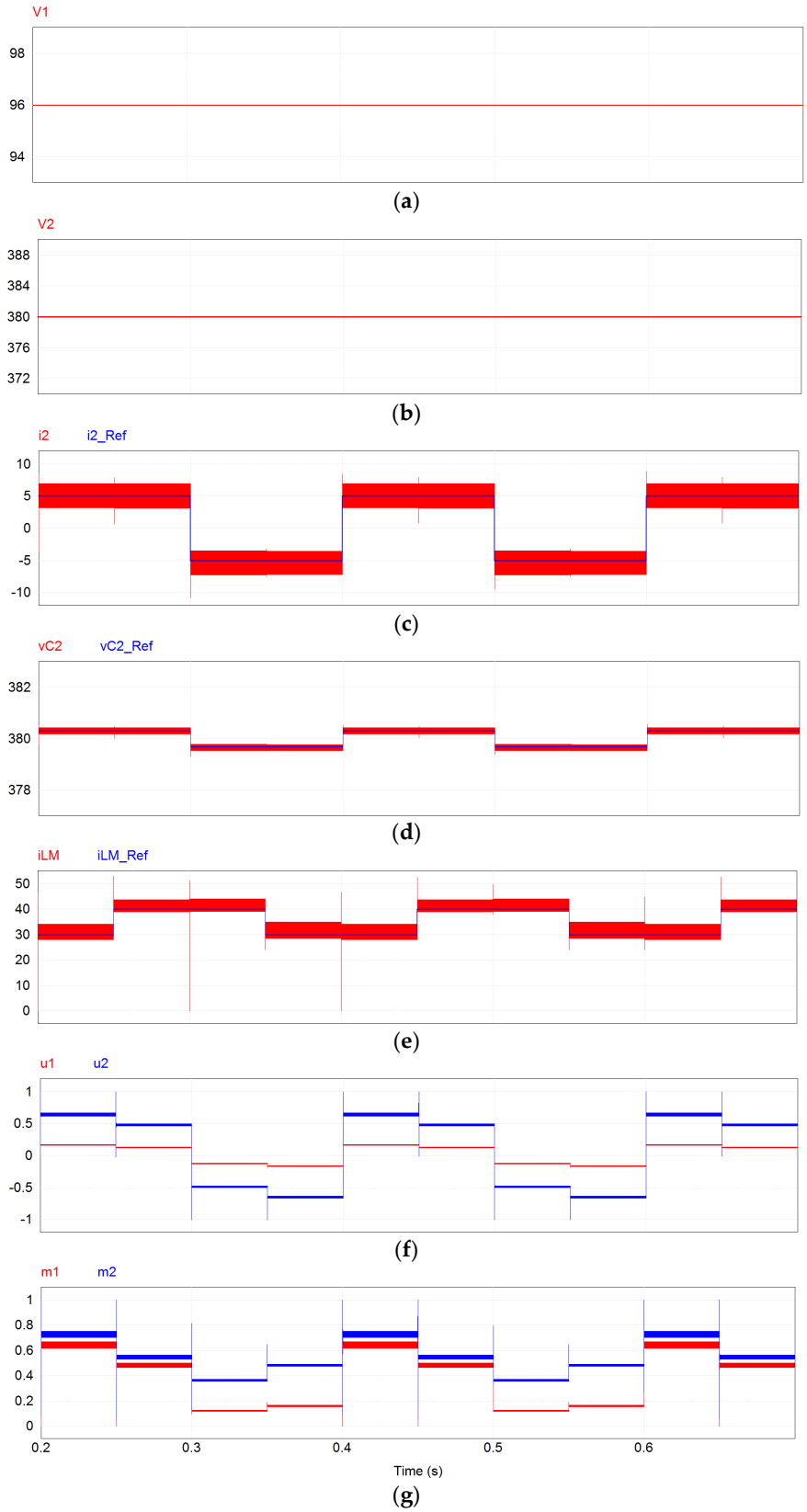

Figure 12. Waveforms for the tri-state buck–boost control with state feedback linearization. (**a**) Voltage at Bus 1 (in V), (**b**) voltage at Bus 2 (in V), (**c**) reference and output current (in A), (**d**) reference and output capacitor voltage (in V), (**e**) reference and inductor current (in A), (**f**) non-linear control variables, (**g**) PWM modulation signals.

Next, Figure 13 presents the results for essentially the same test, but for the converter operating in dual-state mode with the cascaded linear controller. In this case, the output voltage (v_{C2}) is adjusted by varying the inductor current (i_{LM}).

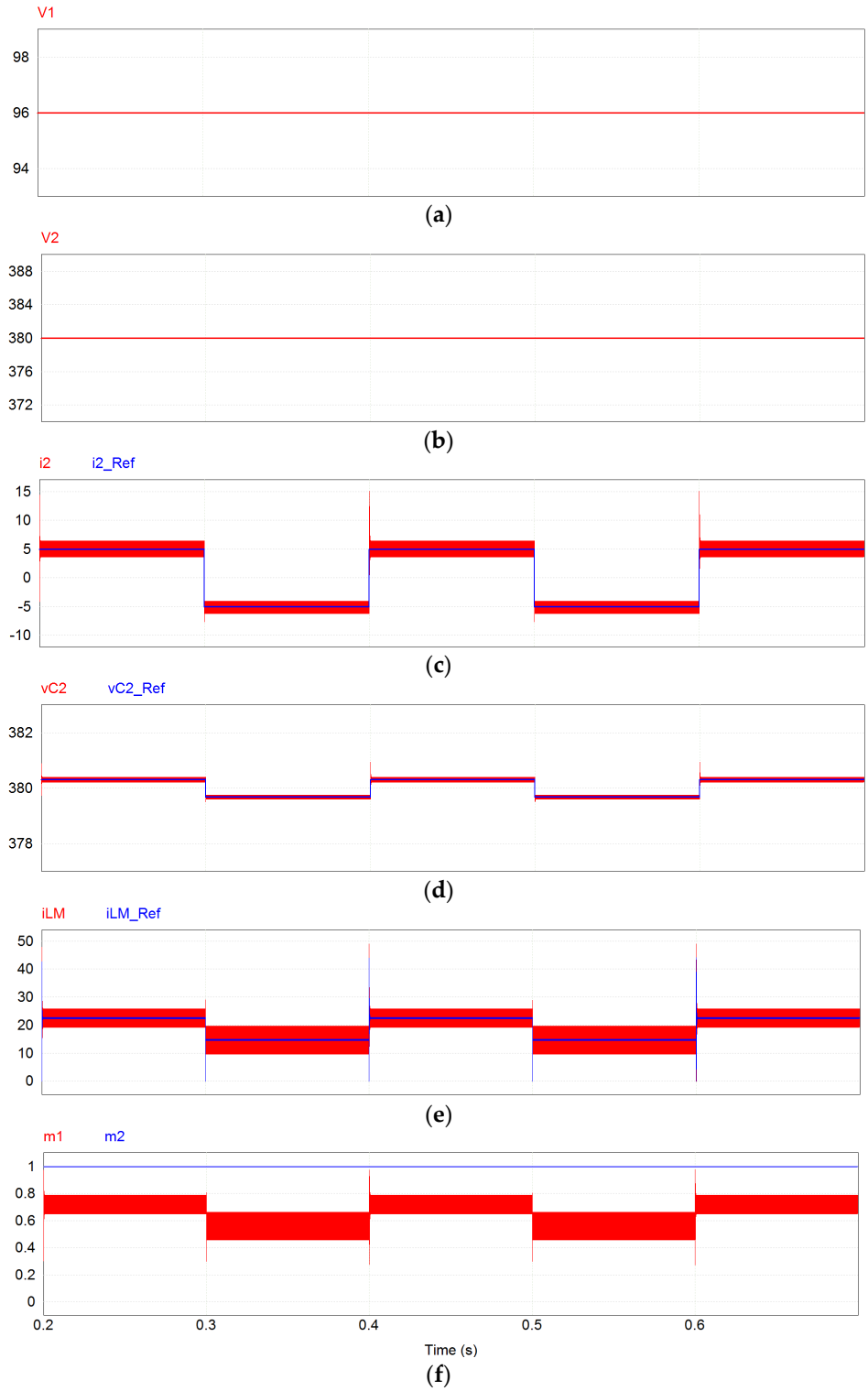

Figure 13. Waveforms for the dual-state buck–boost control with conventional cascaded control loops. (**a**) Voltage at Bus 1 (in V), (**b**) voltage at Bus 2 (in V), (**c**) reference and output current (in A), (**d**) reference and output capacitor voltage (in V), (**e**) reference and inductor current (in A), (**f**) PWM modulation signals.

6.2. Tests with an SC at Bus 1 and Bus 2 with a Sinusoidal Ripple

In this test, the fixed voltages, or "strong buses", previously used in Bus 1 and Bus 2, are replaced, respectively, by an SC (a storage element) and a controlled DC microgrid, which corresponds to another common application for bi-directional DC-DC converters. This concerns a more demanding operating condition where the input (V_1) and output (V_2) voltages of the converter can vary considerably, driving the operating point of the converter further away from the base operating point. There are several papers focused on the sizing of SCs for given applications [29–31], which are typically in the order of 100 s of F. In this particular test, a small supercapacitor (95 mF) was considered for the test so that one can observe the impact of its voltage variation on the response of the inductor current (i_{LM}) and output voltage (v_{C2}) control loops, in a single time frame.

Figure 14 shows some relevant waveforms for this test. In Figure 14a, one sees the DC microgrid voltage at Bus 2 with the 20 V/120 Hz sinusoidal ripple. In Figure 14b, one sees that the output current (i_2) tracks very well the reference signal (i_{2_ref}), a square wave of $\pm$5 A and 5 Hz. The waveform of V_1, the SC voltage at Bus 1, is shown in Figure 14c. It starts at 96 V and decreases due to a positive value for i_2. At t = 0.3 s, it reaches approximately 72 V and starts to increase as the value of i_2 changes to -5 A. Thus, the variation in V_1 and V_2 has no negative impact on the performance of the proposed control scheme. Moreover, v_{C2} in Figure 14d and i_{LM} in Figure 14e track their reference signals accurately. Note that, in this case, the inductor current reference (i_{LM_ref}) was kept constant at 35 A. Good tracking performance was achieved with the waveforms of control variables (u_1 and u_2) shown in Figure 14f and modulation signals (m_1 and m_2) shown in Figure 14g.

The five-switch converter operating with dual-state buck–boost and conventional linear cascaded control loops is subjected to the same test. The results are shown in Figure 15. In Figure 15a, one sees that the DC microgrid voltage waveform at Bus 2 (V_2) is the same as in the test for the non-linear controller. In Figure 15b, one sees that this conventional modulation and control scheme tracks the positive output current reference (i_{2_ref}) well until the moment that the decreasing SC voltage, (V_1 in Figure 15c), reaches a value of approximately 80 V. This is when the modulation signal (m_1) and several waveforms start to oscillate. The control scheme starts to malfunction. At t = 0.3 s, when the power flow reverses and $i_{2\_ref} = -5$ A, the output current (i_2) fails to track it, becoming more negative (lower) than i_{2_ref}. The inductor current (i_{LM}) and inductor current reference (i_{LM_ref}) waveforms, shown in Figure 15e, are limited at the maximum value, 50 A. One sees in Figure 15f that the modulation signal (m_1) decreases following the change of i_{2_ref} to -5 A, but starts to increase, unlike in the previous test for fixed values of V_1 and V_2 (Figure 13f), when its average value remained relatively constant. Overall, as a result of i_2 becoming more negative than i_{2_ref} at t = 0.3 s, V_1 increases more than expected, reaching 140 V at t = 0.4 s. From this point on, the linear controller is able to control the output current, but keeping the input voltage in the range of 120–140 V. In summary, due to the issues in tracking the reference output current/voltage in operating conditions different from the designed ones, the conventional control scheme fails to track the reference output current, which can even lead to damage to the SC and switches, due to overvoltage conditions.

6.3. Results for SC Voltage Falling to Half-Rated Value

For this test, to have the SC voltage decreasing from rated (96 V) to half-rated (48 V) using the same square output current reference (i_{2_ref}) of $\pm$5 A and 5 Hz, the SC used in the previous test is replaced by a smaller one of 55 mF. Figure 16 shows some relevant waveforms for this test. Moreover, since the DC microgrid voltage waveform at Bus 2 (V_2) is the same as in the previous tests, it is omitted in the next figure.

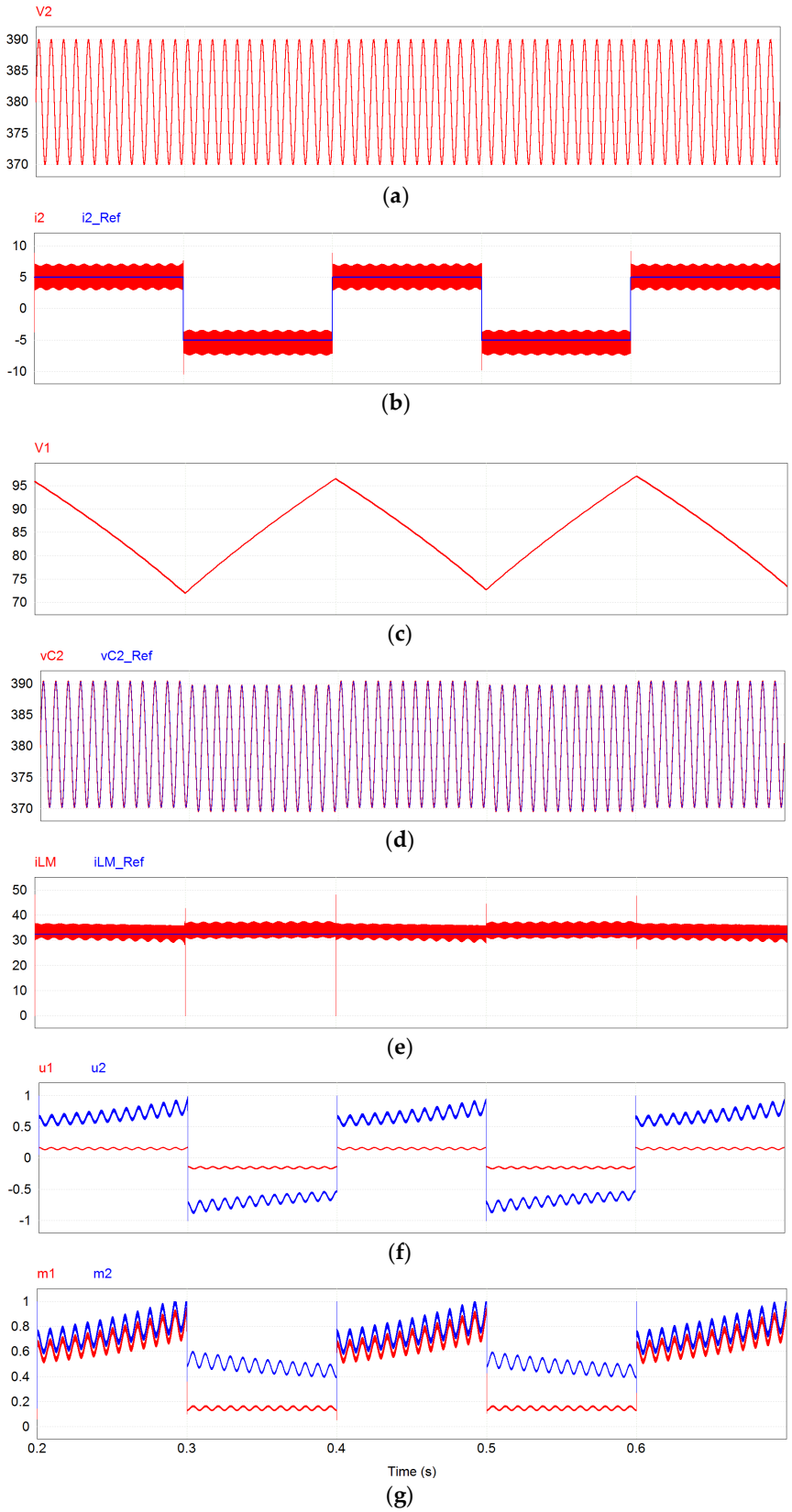

Figure 14. Waveforms for the tri-state buck–boost control with state feedback linearization for test 2. (**a**) Voltage at Bus 2 (in V), (**b**) reference and output current (in A), (**c**) voltage at Bus 1 (in V), (**d**) reference and output capacitor voltage (in V), (**e**) reference and inductor current (in A), (**f**) non-linear control variables, (**g**) PWM modulation signals.

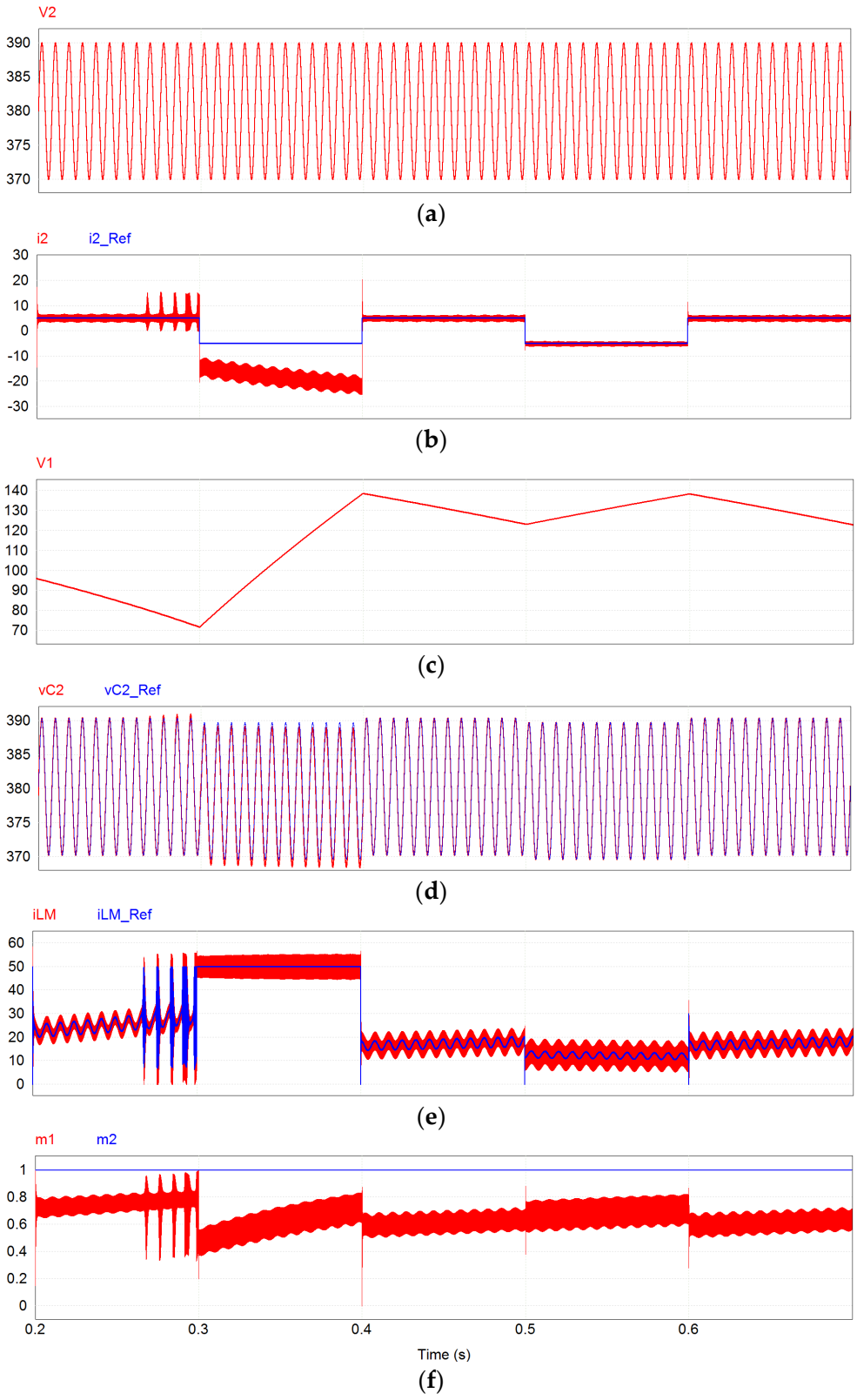

Figure 15. Waveforms for the conventional cascaded control scheme for test 2. (**a**) Voltage at Bus 2 (in V), (**b**) reference and output current (in A), (**c**) voltage at Bus 1 (in V), (**d**) reference and output capacitor voltage (in V), (**e**) reference and inductor current (in A), (**f**) PWM modulation signals.

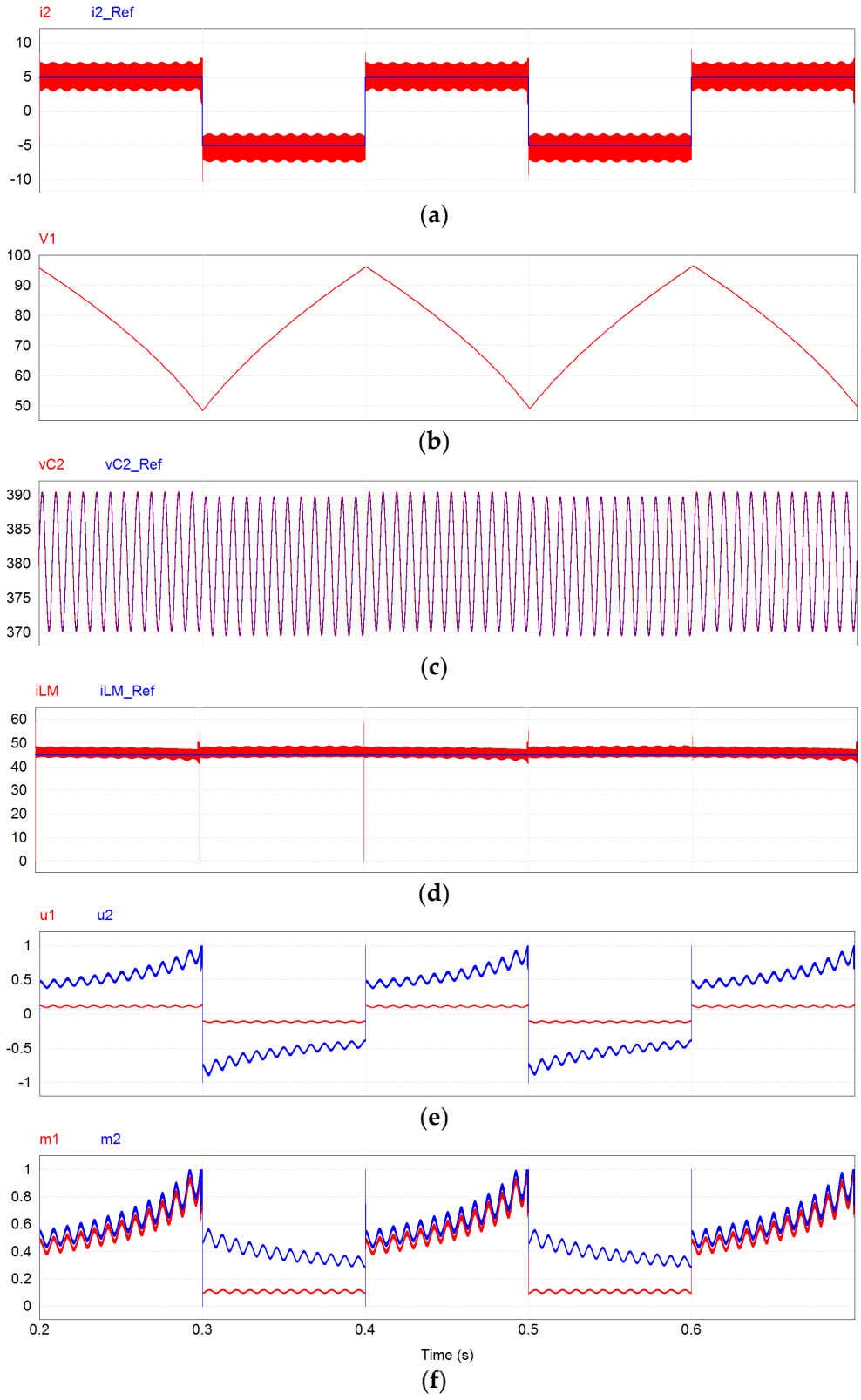

Figure 16. Waveforms for the tri-state buck–boost control with state feedback linearization for test 3. (**a**) Reference and output current (in A), (**b**) voltage at Bus 1 (in V), (**c**) reference and output capacitor voltage (in V), (**d**) reference and inductor current (in A), (**e**) non-linear control variables, (**f**) PWM modulation signals.

In Figure 16a, one sees that the output current waveform (i_2) tracks very well i_{2_ref}. The voltage at the SC (V_1) is shown in Figure 16b. It starts at 96 V and decreases due to the positive value for i_2. At t = 0.3 s, it reaches 48 V and starts to increase as the value of i_2 changes to −5 A. Thus, the larger variation in V_1 has no negative impact on the performance of the proposed control scheme. The output capacitor voltage (v_{C2}) in Figure 16c and the inductor current (i_{LM}) in Figure 16d track their reference signals accurately. Note that in this case, the inductor current reference (i_{LM_ref}) was increased to 45 A in order to avoid the saturation of the control variables, which tend to increase as V_1 decreases. Good tracking performance was achieved with the waveforms of control variables (u_1 and u_2) shown in Figure 16e and modulation signals (m_1 and m_2) shown in Figure 16f.

The results for the conventional dual-state modulation and linear cascaded control loops under the same conditions are shown in Figure 17.

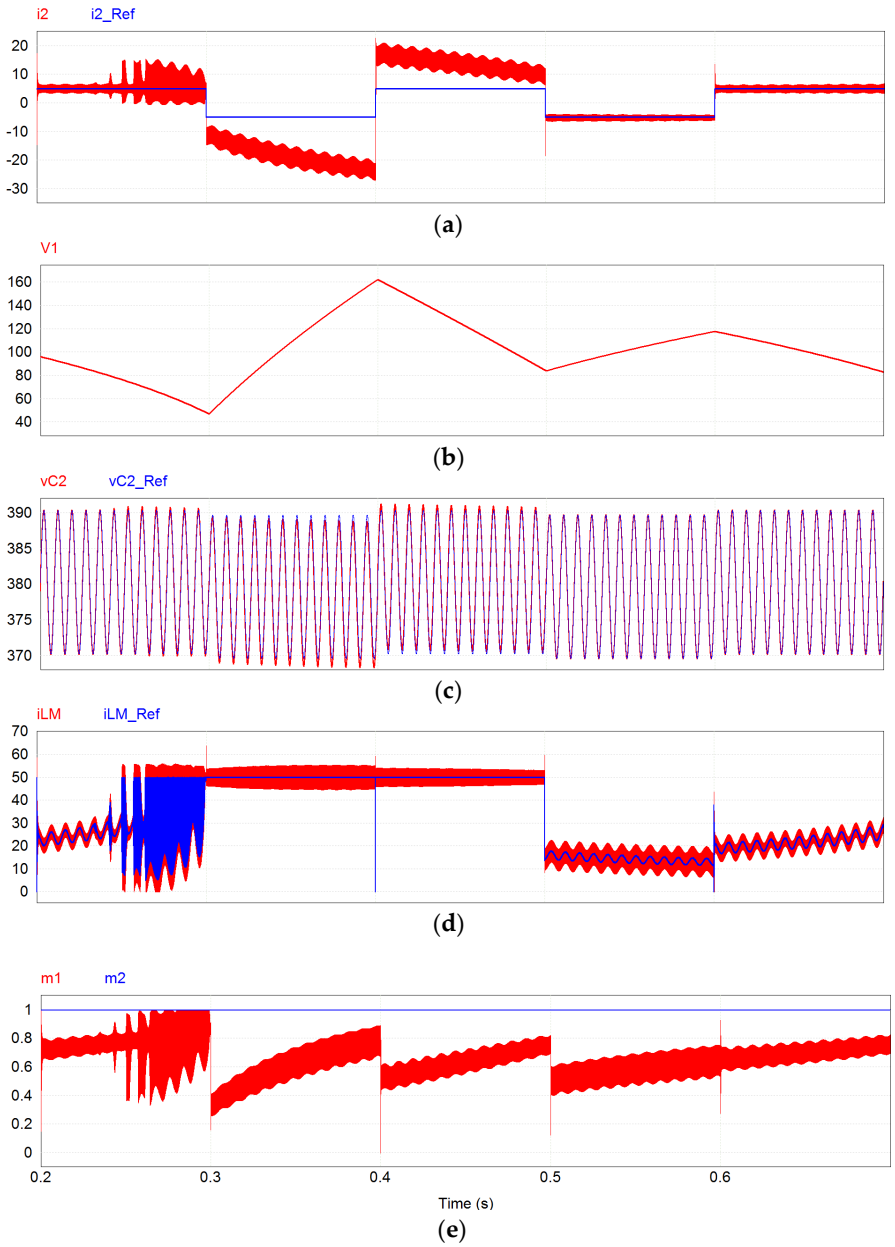

Figure 17. Waveforms for the conventional cascaded control scheme for test 3. (**a**) Reference and output current (in A), (**b**) voltage at Bus 1 (in V), (**c**) reference and output capacitor voltage (in V), (**d**) reference and inductor current (in A), (**e**) PWM modulation signals.

In Figure 17a, one sees that this conventional modulation and control scheme tracks the positive output current reference (i_{2_ref}) well until the moment that the decreasing SC voltage, (V_1 in Figure 17b), reaches a value of approximately 80 V. At this point, similar to the previous test with the slightly larger SC, the modulation signal (m_1) and several waveforms start to oscillate and the control scheme starts to malfunction. At t = 0.3 s, when the power flow reverses and $i_{2\_ref} = -5$ A, the output current (i_2) fails to track it, becoming more negative (lower) than i_{2_ref}. The inductor current (i_{LM}) and inductor current reference (i_{LM_ref}) waveforms, shown in Figure 17d, are limited at the maximum value, 50 A. Overall, as a result of i_2 becoming more negative than i_{2_ref} at t = 0.3 s, V_1 increases more than expected, reaching 160 V at t = 0.4 s. This is when i_{2_ref} becomes positive again but, still, i_2 fails to track it. Nonetheless, V_1 decreases. At t = 0.5 s, when i_{2_ref} becomes -5 A and with V_1 with a value of approximately 85 V, which is close to its rated value (96 V), the conventional control scheme starts to work again, with i_2 tracking i_{2_ref} well, until the end of the test. Again, note that the linear controller is not able to keep the SC voltage within the desired range of 96–48 V.

6.4. Efficiency Estimation

Having shown that the five-switch DC-DC converter operating with tri-state modulation and the proposed non-linear controller behave equally well regardless of the operating point, it is important to assess the impact of such a modulation and control scheme on the power losses. For this, two main sources of losses are considered in this analysis: conduction and switching losses on the semiconductors.

For the conduction losses, recall that switches S_1 to S_4 consist of MOSFETS in series with diodes to realize semiconductor switches that are unidirectional in current, while S_T concerns a MOSFET only. In terms of losses, this means that the conduction losses in such devices (S_1 to S_4) will be defined as the sum of the conduction losses in each semiconductor, while S_T follows the conventional losses calculation for a standard MOSFET. From the power semiconductor theory, one knows that

$$Pcond_{MOSFET} = {i_{S_{RMS}}}^2 R_{DS} \tag{43}$$

$$Pcond_{Diode} = {i_{D_{RMS}}}^2 R_T + i_{D_{AVG}} V_{TO} \tag{44}$$

where R_{DS} and R_T are, respectively, the conduction resistance of the MOSFET and diode, and V_{TO} is the forward voltage of the diode. Subscripts S and D correspond to MOSFET and diode quantities, and RMS and AVG to root-mean-square and average values.

Since the MOSFET and diode are in series, for S_1 to S_4, they have the same values of average and RMS current. Thus, the total conduction losses for S_1 to S_4 can be defined as

$$Pcond_{SD} = {i_{SD_{RMS}}}^2 (R_{DS} + R_T) + i_{SD_{AVG}} (V_{TO}) \tag{45}$$

For the switching losses, the following equations, (46) and (47), are used for the calculations. One important detail for the switching loss estimation is that, if the voltage across the series connection of the MOSFET and the diode is positive, the losses will be all concentrated in the MOSFET; thus, for this case, $Psw_{Diode} = 0$. Likewise, if the voltage across the series connection of the MOFEST and the diode is negative, the losses will be all concentrated in the diode; thus, for this case, $Psw_{MOSFET} = 0$.

$$Psw_{MOSFET} = f_s V_{DS} \frac{\left(t_f i_{s_{rise}} + t_r i_{s_{fall}} \right)}{2} + f_s V_{DS} k_{oss} \tag{46}$$

$$Psw_{Diode} = f_s V_D Q_{RR} \tag{47}$$

where f_s is the switching frequency; t_f and t_r are, respectively, the rise and fall times of the MOSFET; k_{oss} is the coefficient related to the losses due to the output capacitance C_{oss} of the

MOSFET; Q_{RR} is the coefficient related to the losses due to the reverse recovery time of the diode.

From the above equations, one sees that it is necessary to obtain the RMS and average currents of the switches/diodes and maximum voltage of the switches (V_{DS}) and the diodes (V_D). This can be derived from the information presented in Table 1 and the analysis of the operating states presented in Figures 2 and 3. Moreover, it is important to select suitable power devices that match the power ratings of the desired application. Considering the voltage and current levels of the case studies discussed previously, Table 2 presents the devices chosen for this loss estimation analysis.

Table 2. Power semiconductors chosen for this study.

Components	Devices	Parameters
S_1 to S_4 and S_T	5× IPW90R120C3 (900 V/36 A)	R_{DS} = 0.12 Ω; t_f = 25 ns; t_r = 20 ns; k_{oss} = 3.9855 × 10^{-8} J/V
D_1 to D_4	4× FFSH30120A (1200 V/30 A)	R_T = 0.013 Ω; V_{TO} = 1.45 V

The final plots considering the estimated efficiency of each mode/power flow direction, as a function of the output current, are presented next. This can be seen in Figures 18 and 19.

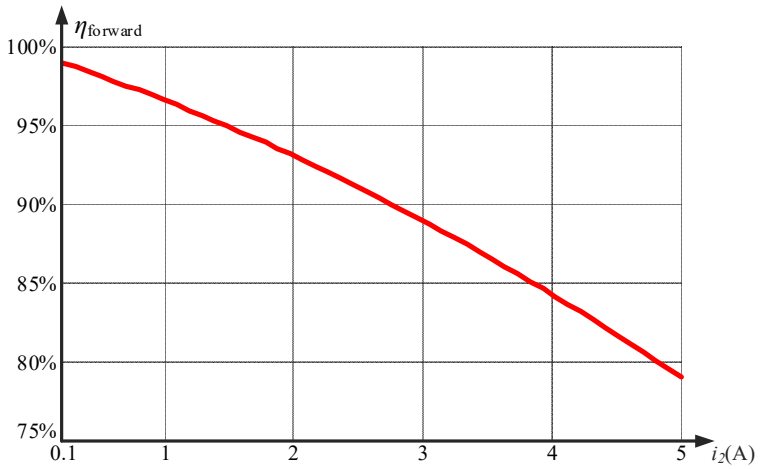

Figure 18. Efficiency estimation for the forward mode.

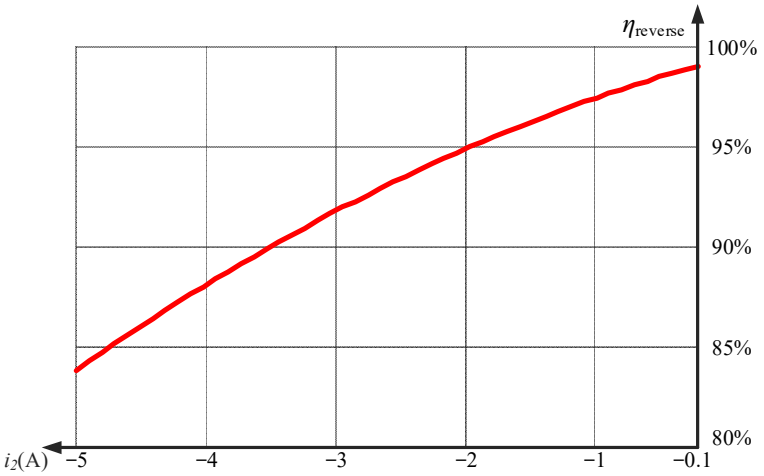

Figure 19. Efficiency estimation for the reverse mode.

As can be seen from Figures 18 and 19, as the output current increases its absolute value, the efficiency of the system tends to drop, which is to be expected, since larger values of output current should increase the RMS and average values of the currents flowing through the semiconductors. Although the efficiency for low output currents is virtually the same for both modes, another aspect to be highlighted is the fact that, as the output current increases its absolute value, the reverse mode presents lower power losses, thus presenting higher efficiency than the forward mode. This can be explained by the fact that, for the reverse mode, the high-voltage side is the one directly connected to the primary winding of the tapped inductor, which means that the lower average current of this DC bus results in a smaller current ripple for the magnetizing current, thus lowering the losses of the overall system.

It should be noted that the power loss/efficiency estimation is performed taking into consideration the power devices presented in Table 2, where one possible option would be to select, depending on the availability, power devices with better characteristics for increased efficiency of operation.

7. Conclusions

The performance of energy storage systems (ESSs), in terms of the dynamic response and tracking of the reference output current, depends on the features of the power converter and control scheme. This paper presented the modeling of a novel five-switch DC-DC power converter, which presents a high voltage gain (V_2/V_1) and does not require the reversal of the intermediate inductor current to achieve power flow reversal. In terms of the control scheme, by operating this converter in a tri-state buck–boost mode, one eliminates the right half-plane (RHP) zero from the output-to-control transfer function, which facilitates the design of the control loop. Moreover, by employing the exact state feedback linearization technique, the converter should be able to operate in a wider range than that with a PI controller designed considering the conventional small-signal model of the converter. A systematic approach for modeling the converter and obtaining a control law with exact feedback linearization was presented. Note that since the inductor current, a state variable, does not need to reverse during power flow reversal in this particular converter, there will be not potential issues of "divide by zero" in the control law.

The performance of the five-switch DC-DC power converter with the proposed modulation (tri-state buck–boost) and control scheme (exact state feedback linearization) was verified by means of simulations. The selected application was as the interface of a supercapacitor (SC)-based ESS to an output DC bus, such as a DC microgrid. It was compared to the converter operating in the conventional dual-state buck–buck mode with linear cascaded current control loops. As expected, both control schemes present similar good behavior at the operating point that the conventional scheme was designed for. When the input voltage (V_1) varies even moderately, which is common in SC-based ESSs, the conventional scheme fails to track the output current reference. Conversely, the proposed modulation and control scheme tracks accurately, with a good dynamic response and zero steady-state error, the output current reference even with the SC voltage varying in a wide range, from rated to half-rated. This is an important feature of the interfaces of SC-based ESSs that is difficult to obtain with conventional power converters and control schemes.

Directions for Further Development

Having validated the mathematical model and proposed a control scheme for the five-switch bi-directional DC-DC converter, the next step is experimental verification. In this way, other aspects, such as the efficiency, power density and electromagnetic compatibility (EMC), of the converter can be assessed. As power semiconductor switches, MOSFETs, with their fast switching speeds and low R_{DS}(ON), are the natural choice. For switches S_1 to S_4 series diodes, to match the switching speeds of MOSFETs, devices with fast switching characteristics and low reverse recovery times, such as Schottky diodes, should be added to the MOSFETs to provide the unidirectional current, or reverse blocking, feature. Regarding

the proposed control scheme and PWM modulator, the TMS320F28035 microcontroller from Texas Instruments provides the means for its realization. Note that these are common choices for DC-DC converters used as interfaces of distributed energy resources.

Author Contributions: Conceptualization, G.R.B., L.A.C.L. and G.D.; methodology, L.A.C.L. and G.D.; software, G.R.B. and L.A.C.L.; validation, G.R.B., L.A.C.L. and G.D.; formal analysis, L.A.C.L. and G.D.; investigation, G.R.B., L.A.C.L. and G.D.; resources, L.A.C.L.; data curation, G.R.B.; writing—original draft preparation, G.R.B., L.A.C.L. and G.D.; writing—review and editing, G.R.B., L.A.C.L. and G.D.; visualization, G.R.B., L.A.C.L. and G.D.; supervision, L.A.C.L.; project administration, L.A.C.L.; funding acquisition, L.A.C.L. All authors have read and agreed to the published version of the manuscript.

Funding: This research was funded by the Natural Sciences and Engineering Research Council (NSERC) of Canada: DG-N00863.

Conflicts of Interest: The authors declare no conflict of interest.

References

1. Ghareeb, A.T.; Mohamed, A.A.; Mohammed, O.A. DC Microgrids and Distribution Systems: An Overview. In Proceedings of the IEEE Power & Energy Society General Meeting 2013, Vancouver, BC, Canada, 21–25 July 2013; pp. 1–6.
2. Diaz, E.R.; Savaghebi, M.; Vasquez, J.C.; Guerrero, J.M. An overview of low voltage dc distribution systems for residential applications. In Proceedings of the ICCE-Berlin 2015—5th International Conference on Consumer Electronics, Berlin, Germany, 6–9 September 2015; pp. 318–322.
3. Dragicevic, T.; Lu, X.; Vasquez, J.C.; Guerrero, J.M. DC Microgrids—Part I: A Review of Control Strategies and Stabilization Techniques. *IEEE Trans. Power Electron.* **2016**, *31*, 4876–4891. [CrossRef]
4. Dragicevic, T.; Lu, X.; Vasquez, J.C.; Guerrero, J.M. DC Microgrids—Part II: A Review of Power Architectures, Applications, and Standardization Issues. *IEEE Trans. Power Electron.* **2016**, *31*, 3528–3549. [CrossRef]
5. Jing, W.; Lai, C.H.; Wong, S.H.W.; Wong, M.L.D. Battery-supercapacitor hybrid energy storage system in standalone DC microgrids: A review. *IET Renew. Power Gener.* **2017**, *11*, 461–469. [CrossRef]
6. Ferahtia, S.; Djeroui, A.; Mesbahi, T.; Houari, A.; Zeghlache, S.; Rezk, H.; Paul, T. Optimal Adaptive Gain LQR-Based Energy Management Strategy for Battery–Supercapacitor Hybrid Power System. *Energies* **2021**, *14*, 1660. [CrossRef]
7. Bocklisch, T. Hybrid Energy Storage Systems for Renewable Energy Applications. In Proceedings of the IRES 2015—9th International Renewable Energy Storage Conference, Düsseldorf, Germany, 9–11 March 2015; pp. 103–111.
8. Williams, B.W. Unified synthesis of tapped-inductor DC-to-DC converters. *IEEE Trans. Power Electron.* **2013**, *10*, 5370–5383. [CrossRef]
9. Broday, G.R.; Nascimento, C.B.; Agostini, E.; Lopes, L.A.C. A tri-state bidirectional buck-boost converter for a battery/supercapacitor hybrid energy storage system in electric vehicle applications. In Proceedings of the VPPC 2015—IEEE Conference on Vehicle Power and Propulsion, Montreal, Canada, 19–22 October 2015; pp. 1–6.
10. Viswanathan, K.; Oruganti, R.; Srinivasan, D. A Novel Tri-State Boost Converter with Fast Dynamics. *IEEE Trans. Power Electron.* **2002**, *17*, 677–683. [CrossRef]
11. Broday, G.R.; Lopes, L.A.C. A novel 5-switch tapped-inductor multi-state bidirectional DC-DC converter. In Proceedings of the ICIT 2018—IEEE International Conference on Industrial Technology, Lyon, France, 20–22 February 2018; pp. 596–599.
12. Broday, G.R.; Damm, G.; Pasillas-Lépine, W.; Lopes, L.A.C. Modeling and dynamic feedback linearization of a 5-switch tri-state buck-boost bidirectional DC-DC converter. In Proceedings of the ICIT 2021—IEEE International Conference on Industrial Technology, Valencia, Spain, 10–12 March 2021; pp. 427–432.
13. Georgious, R.; Garcia, J.; Sumner, M.; Saeed, S.; Garcia, P. Fault Ride-Through Power Electronic Topologies for Hybrid Energy Storage Systems. *Energies* **2020**, *13*, 257. [CrossRef]
14. Luo, X.; Barreras, J.V.; Chambon, C.L.; Wu, B.; Batzelis, E. Hybridizing Lead–Acid Batteries with Supercapacitors: A Methodology. *Energies* **2021**, *14*, 507. [CrossRef]
15. Yuan, C.; Huangfu, Y.; Ma, R.; Zhao, B.; Bai, H. Nonlinear PI and Finite-time Control for DC-DC Converter Based on Exact Feedback Linearization. In Proceedings of the IECON 2019—45th Annual Conference of the IEEE Industrial Electronics Society, Lisbon, Portugal, 14–17 October 2019; pp. 6398–6403.
16. Callegaro, L.; Ciobotaru, M.; Pagano, D.; Fletcher, J. Feedback Linearization Control in Photovoltaic Module Integrated Converters. *IEEE Trans. Power Electron.* **2019**, *34*, 6876–6889. [CrossRef]
17. Ding-xin, S. State feedback exact linearization control of Buck-Boost converter. In Proceedings of the PEAC 2014—International Power Electronics and Application Conference and Exposition, Shanghai, China, 5–8 November 2014; pp. 1490–1494.
18. Iovine, A.; Carrizosa, M.J.; Damm, G.; Alou, P. Nonlinear Control for DC Microgrids Enabling Efficient Renewable Power Integration and Ancillary Services for AC grids. *IEEE Trans. Power Electron.* **2018**, *34*, 5136–5146. [CrossRef]
19. Perez, F.; Iovine, A.; Damm, G.; Ribeiro, P. DC Microgrid Voltage Stability by Dynamic Feedback Linearization. In Proceedings of the ICIT 2018—IEEE International Conference on Industrial Technology, Lyon, France, 20–22 February 2018; pp. 129–134.

20. Broday, G.R.; Damm, G.; Pasillas-Lépine, W.; Lopes, L.A.C. A Unified Controller for Multi-State Operation of the Bi-Directional Buck–Boost DC-DC Converter. *Energies* **2021**, *14*, 7921. [CrossRef]
21. Gonzalez, A.; Lopez-Erauskin, R.; Gyselinck, J.; Kei Chau, T.; Ho-Ching Lu, H.; Fernando, T. Nonlinear MIMO control of interleaved three-port boost converter by means of state-feedback linearization. In Proceedings of the PEMC 2018—IEEE 18th International Power Electronics and Motion Control Conference, Budapest, Hungary, 26–30 August 2018; pp. 164–169.
22. Cai, P.; Wu, X.; Sun, R.; Wu, Y. Exact feedback linearization of general four-level buck DC-DC converters. In Proceedings of the CCDC 2017—29th Chinese Control and Decision Conference, Chongqing, China, 28–30 May 2017; pp. 4638–4643.
23. Broday, G.R.; Lopes, L.A.C. A Minimum Power Loss Approach for Selecting the Turns Ratio of a Tapped Inductor and Mode of Operation of a 5-Switch Bidirectional DC-DC Converter. In Proceedings of the ICDCM 2021—IEEE 4th International Conference on DC Microgrids, Arlington, USA, 18–21 July 2021; pp. 1–7.
24. Lee, D.-C.; Lee, G.-M.; Lee, K.-D. DC-bus voltage control of three-phase AC/DC PWM converters using feedback linearization. *IEEE Trans. Ind. Applic.* **2000**, *36*, 826–833.
25. Lu, Z.; Zhang, X.; Wang, Y. Nonlinear Control Strategy of Hybrid Energy Storage Systems Based on Feedback Linearization. In Proceedings of the CVCI 2020—4th CAA International Conference on Vehicular Control and Intelligence, Hangzhou, China, 18–20 December 2020; pp. 674–677.
26. Ming, W.; Liu, J. A new experimental study of input-output feedback linearization based control of Boost type DC/DC converter. In Proceedings of the ICIT 2010—IEEE International Conference on Industrial Technology, Viña del Mar, Chile, 14–17 March 2010; pp. 685–689.
27. Li, X.; Chen, X. A Multi-Index Feedback Linearization Control for a Buck-Boost Converter. *Energies* **2021**, *14*, 1496. [CrossRef]
28. Ogata, K. *Modern Control Engineering*; Prentice Hall: Hoboken, NJ, USA, 2010.
29. Abeywardana, D.B.W.; Hredzak, B.; Agelidis, V.G.; Demetriades, G.D. Supercapacitor Sizing Method for Energy-Controlled Filter-Based Hybrid Energy Storage Systems. *IEEE Trans. Power Electron.* **2017**, *32*, 1626–1637. [CrossRef]
30. Dotelli, G.; Ferrero, R.; Stampino, P.G.; Latorrata, S.; Toscani, S. Supercapacitor Sizing for Fast Power Dips in a Hybrid Supercapacitor-PEM Fuel Cell System. *IEEE Trans. Intrum. and Meas.* **2016**, *32*, 2196–2203. [CrossRef]
31. Arnaudov, D.; Punov, P.; Dimitrov, V. Supercapacitor Sizing for Power Defined Loads. In Proceedings of the ET 2019—IEEE XXVIII International Scientific Conference Electronics, Sozopol, Bulgaria, 12–14 September 2019; pp. 1–3.